Thermal neutron radiography of a passive proton exchange membrane fuel cell for portable hydrogen energy systems

M. Chaparro, A.; Ferreira-Aparicio, P.; Folgado, M. A.; Hübscher, R.; Lange, C.; Weber, N.;

Originally published:

September 2020

Journal of Power Sources 480(2020), 228668

DOI: https://doi.org/10.1016/j.jpowsour.2020.228668

Perma-Link to Publication Repository of HZDR:

https://www.hzdr.de/publications/Publ-31084

Thermal neutron radiography of a passive proton exchange membrane fuel cell for portable hydrogen energy systems

Rico Hübscher[(1)], Carsten Lange[(1)], Norbert Weber[(2)], M. Antonia Folgado[(3)], P. Ferreira-Aparicio[(3)], Antonio M. Chaparro[(3),*]

(1) TU Dresden. Faculty of Mechanical Science and Engineering. Institute of Power Engineering. 01062 Dresden. Germany.
(2) Institut für Fluiddynamik. Helmholtz-Zentrum Dresden-Rossendorf e.V. Bautzner Landstr. 400, 01328 Dresden. Germany
(3) Dep. of Energy. CIEMAT. Avda. Complutense, 40. 28040 Madrid. Spain

Abstract

A proton exchange membrane fuel cell (PEMFC) for low power and portable applications is studied with thermal neutron radiography. The portable PEMFC consists of a passive air-breathing cathode and a dead-end anode, supplied with static ambient air and dry hydrogen, respectively. Neutron images are used to study liquid water accumulation in the cell body, complemented with polarization curves and impedance spectroscopy. The passive cells are studied in vertical and horizontal orientations, with their main plane aligned parallel and perpendicular to the gravity field, respectively. Preferential water accumulation is observed in the grid contacts and the cathode surface of the cells. In vertical position, the cells show lower water saturation inside the pores of the cathode and improved oxygen transport, as observed from cross sectional water profiles, and inferred from the analysis of polarization curves and impedance spectra. The vertical position favors liquid water transport by large drops rolling over the cathode surface and by the onset of natural convection. As a consequence, the vertical cell can be operated continuously, without performance loss, providing a steady peak power density of 90 mW cm^{-2}, at 35 - 40 °C, and under full passive conditions. In contrast, gravity and natural convection are less effective for water transport in horizontal position, leading to larger mass transport losses and a 17 % decrease in peak power density. The horizontal position is especially adverse when the upper electrode is the cathode because of anode flooding, which causes cell failure after production of a small amount of water (5 mg cm^{-2}). The combined information from thermal neutron radiography and cell response characteristics shows an important influence of cell orientation on water transport and performance of a fully passive air-breathing PEMFC for portable applications.

Keywords: PEMFC, hydrogen, fuel cell, neutron radiography, water transport, portable fuel cell

1. Introduction

Over the last two decades, the development of hydrogen fuel cells has attained sufficient maturity for low power and portable applications which benefit from their high power density and safety [1,2,3,4,5,6,7]. However, particular operation conditions in portable applications dictate changes in the design of the cells [8]. Very often, they must operate in proximity to the user, so the cell should not compromise personal comfort, and safety, by the emission of heat, liquid water, or noise. In addition,

portability requires large autonomy, compact, and light-weight power production systems.

Using a passive air breathing cathode is a necessary change for the design of a low power portable fuel cell [9,10,11,12], working with static ambient air and passive rejection of water. There is no convective force applied for oxygen and water transports, but only the natural forces like the originating ones from concentration and heat gradients, water evaporation-condensation, and gravity drag of water drops over the cathode surface. The portability of the PEMFC improves if a passive anode is used in front of the air-breathing cathode. The passive anode operates in dead-end mode and under a static atmosphere of dry hydrogen. It must also reject the excess water back-diffused from the cathode to avoid flooding. For this reason, the passive anode requires the implementation of passive water rejection elements, conveniently disposed to maintain gas tightness, like the use of superhydrophobic layers that repeal the liquid water from its porous structure [13], or a hydrophilic membrane to allow its permeation to the outside [14]. It will provide larger hydrogen usage and longer autonomy together with a decrease in auxiliary consumptions.

A complete anode and cathode passive cell design has been recently developed and tested able to operate under static hydrogen and air atmospheres [15]. The full passive cell combines the air-breathing cathode with a passive anode allowing for uninterrupted power production with static air atmosphere and dry hydrogen feeding. **Fig. 1** shows schematically the fundamental differences between the conventional and the fully passive PEMFC. The conventional cell operates under a flow of hydrogen and oxygen/air parallel to the electrodes surfaces, which accelerates liquid water transport and elimination from the cell (Fig.1a). The hydrogen in the anode flows by the periodical purging and recirculation circuit, while an air stream over the cathode surface is applied by pumps or fans. Gas flows are conveniently channeled with flow field plates at the back of the electrodes, which also help for the rejection of water, current collection, and clamping pressure application. This configuration allows for large power production rates, without water transport limitation except at very high current densities, at the expense of additional elements and consumptions. The passive feeding PEMFC (Fig. 1b) operates without active convection in the electrodes and without flow field plates, which decreases water rejection rate and gross power generation, but avoids extra consumptions and auxiliary elements. The choice for one or the other configuration basically depends on power production and operation requirements of the application [7].

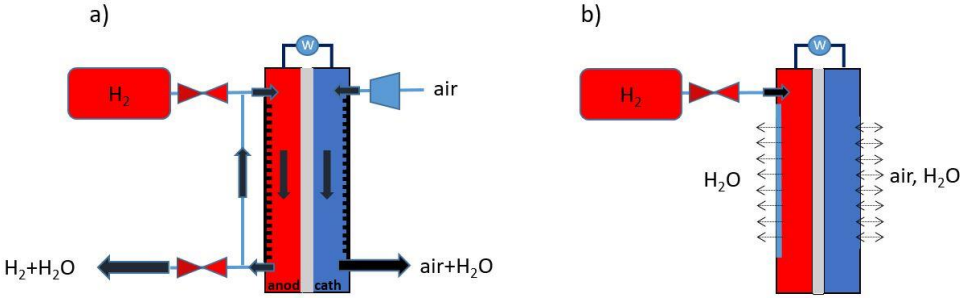

Fig. 1. Schemes of a) conventional, and b) fully passive PEMFC configurations.

Continuous power production by a passive PEMFC relies on the effective rejection of water produced in the cathode catalyst layer, which may accumulate and flood its pores causing large voltage losses. A fraction of water from cathode is rejected towards the anode, where flooding is even more critical due to the lower solubility of

hydrogen than oxygen (0.16 mg/100 g_{H2O} vs. 4.1 mg/100 g_{H2O} at 20 °C and 1 atm) [16]. On the cathode surface, water elimination by gravity drag, evaporation, and/or natural convection are essential to maintain power production. Parameters of the electrode like morphology, pores size distribution, thickness, hydrophobicity, and plate design, are critical to maximize the water removal rate. System packaging and surrounding conditions, like temperature and humidity, have also a strong influence on the performance of a passive PEMFC, which must attain a delicate intermediate state between flooding and dry-out [17,18]. Fabian et al. plotted contour maps of the power density and water accumulated as a function of ambient parameters, showing that optimal performance of the passive cell is a complex function of ambience, load conditions, and cell design [19]. The management of liquid water limits power production under a wide range of operation conditions, wider than for a conventional flow-field PEMFC, and is critical for continuous and optimal passive PEMFC operation.

A technique that provides most useful information of water dynamics in a PEMFC is neutron radiography. Neutrons have a high sensitivity to liquid water inside porous structures and solid volumes. High lateral and temporal resolutions can be attained, with pixel sizes as low as 30 µm and image acquisition times from 5 s. Studies in-operando have been carried out with conventional PEMFC [20,21,22,23,24,25], and passive air-breathing PEMFC [10,26]. In conventional cells, many studies have shown the water accumulation in the channels of the flow field plates as a function of cell design and operation parameters. Siegel et al. [20] showed water accumulation and voltage drop in the anode and cathode of a cell fed with dry hydrogen and periodical purging. Studies at high current densities show intense water accumulation under the ribs of flow field plates leading to transport losses parallel and perpendicular to the cell plane [21], and dependent on cell compression [24]. The influence of the gas flow configuration in a water cooled commercial stack has been studied by Iranzo et al. by combining neutron radiography with localized temperature, current density, and modelling [24]. Beyond the flow field channels, liquid water observation has been possible inside the gas diffusion layer by dark field neutron imaging with a grating interferometer [27]. Some studies of neutron imaging have been carried out on passive air-breathing cells. Weiland et al. studied cells changing the number and size of openings in the cathodic plate [10]. They found accumulation of the water produced by the cell only in the cathode, not in the anode, and attribute voltage losses to the obstruction of openings. Coz et al. [26] studied water management in a planar air-breathing stack fabricated on printed circuit board, and delivering up to 150 mW cm^{-2}; their cell design showed heterogeneous water accumulation in the anode and cathode that leads to 50% loss in performance after ten hours of operation. In addition to neutron radiography, other techniques used for in-operando liquid water studies of PEMFCs are the X-ray radiography [28,29,30,31,32,33], droplet microvisualization inside optically transparent cells [34], and nuclear magnetic resonance [35], some of them requiring changes in cell configuration that may alter operation characteristics [36].

In this work, neutron radiography is used for the in-operando study of a passive PEMFC for portable applications. The PEMFC has optimized electrode and cell design for operation with fully static hydrogen and ambient air. Neutron imaging experiments have been performed keeping the original design almost unmodified, except for the use of aluminum plates, which are almost transparent to thermal neutrons, instead of plastic plates. Cells are studied in vertical and horizontal positions to observe how gravitational force and natural convection determine passive water transport and

performance. Results are complemented with polarization curves and impedance spectroscopy.

2. Experimental

2.1 Passive PEMFC description

Characteristics of the passive PEMFC design are shown in **Fig. 2a**, and the scheme of operation in **Fig. 2b**. The cell has a circular design with an active area of 7.1 cm^2, and optimized anode and cathode architectures for passive operation. The anodic plate is a perforated disk made of aluminum alloy (SIMAGALTOK 82 EN AW 6082, 5mm thickness, 5cm diameter) that allocates a gas diffusion electrode (GDE) (ELAT GDE LT250EWALTSI, BASF, 0.25 mg_{Pt} cm^{-2}) and an Au covered Ni grid (Dexmet) current collector. For gas tightness, the collector grid is framed with 3D printed PLA and sealed with silicone gaskets. A hydrophilic membrane (Nafion 117, Ion Power Inc.) is placed at the back of the perforated anodic plate to help for the passive liquid water removal from the anode (Fig. 2b). The cathode is open air and consists of an aluminum columnar plate (adapted from a pin heatsink, Fischer Elektronik), an Au covered Ni grid (Dexmet), and a GDE (W1S1009, FuelCellsEtc., 0.30 mg_{Pt} cm^{-2}). The electrolyte is a Nafion 212NR membrane (Ion Power Inc.). All cell elements except the cathodic plate, i.e. the anodic plate, GDEs, membrane, and the two grid contacts, are tightened with eight stainless steel bolts (M3) and nuts at 1 N m torque; the cathodic plate is tightened independently with another set of nuts at 0.5 N m torque.

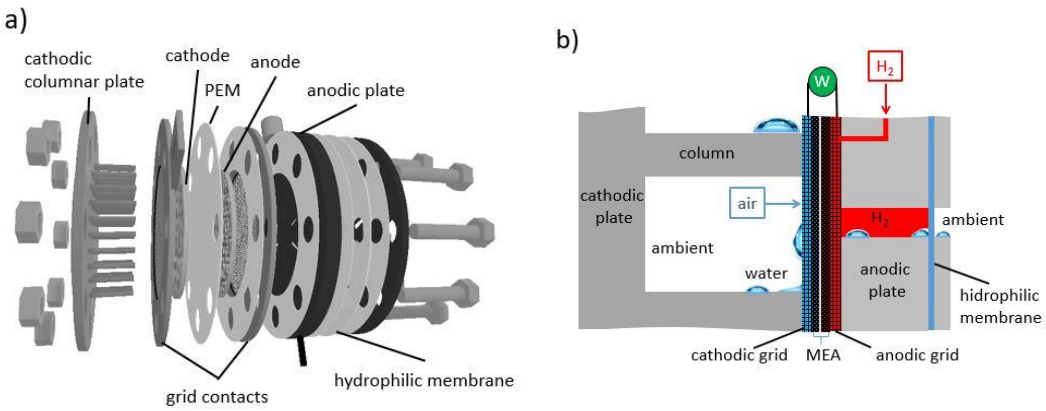

Fig. 2. a) Exploded view of the passive PEMFC components; b) scheme of the passive operation.

2.2 Electrochemical characterization

The cell response was studied with polarization curves and impedance spectroscopy under static ambient air conditions with controlled temperature and humidity at 22 °C and 30 % RH, respectively, inside a climatic chamber (Dycometal). Cells were supplied with 0.5 bar_g static hydrogen (Air Liquide, 99.999 %) in the anode, and ambient air in the cathode. Polarization curves were obtained potentiostatically (Autolab 30 N with 10 A current booster), by stepping cell voltage from open circuit to 0.3 V, at 10 mV s^{-1} and 2.4 mV steps. Before the acquisition of the curves, cells were brought to and kept in a steady-state by polarizing at 0.5 V during 30 min until constant current and temperature were attained. During the measurement of the polarization curve, the ventilator of the climatic chamber was switched-off to allow for a fully static ambient air. Impedance spectroscopy measurements were carried out potentiostatically (sine wave, V_{ac} = 10 mV_{RMS}) from 20 kHz to 0.1 Hz (50 points), with the cells placed inside the

climatic chamber and ventilator switched-off during measurements. Previous to impedance acquisition, the cell is set at the predetermined potential until its temperature and current response are stabilized. Kronig-Kramer tests and equivalent circuit analysis were carried out on impedance spectra with Autolab software (Nova). Kronig-Kramer tests, to check stability and linearity conditions, were satisfactorily passed for all spectra presented. The temperature of the cells was monitored during measurements by means of a thermocouple put in contact with the cathodic plate.

2.3 Neutron radiography

2.3.1 Thermal neutron source and imaging set-up. Neutron imaging of an in-operando fuel cell with thermal neutrons was performed for the first time at the training and research reactor AKR-2 of the Technische Universität Dresden [37]. The AKR-2 is a very low flux, thermal, homogeneous, solid moderated zero-power reactor with a maximum continuous power of 2 W. Nuclear fission is mainly caused by thermal neutrons, i.e. neutrons with the same kinetic energy as the particles of ambient materials. The nuclear fuel and moderator material (solid polyethylene) is distributed homogeneously in fuel plates. Radial channel 7 was used for best combination of exposure time and effective beam divergence, with an absolute thermal neutron flux of Φ = 2300 n cm^{-2} s^{-1} (±5%). The raw data of the neutron radiographs were taken with an upgraded system containing an Andor iKon-M 934 (1024x1024 pixels) camera cooled down to -70 °C combined with a light tight DNIDS box provided by Paul-Scherrer-Institute, a Nikkor AF-S 50 mm 1:1,4G lens and a 200 µm thick ^{6}LiF/ZnS(Ag) scintillator from Tritec. The effective pixel size has been estimated to be about 0.133 mm, which results in a spatial resolution of 0.266 mm (see also Supplementary Information, S1). The effective spatial resolution will depend on additional influences, like scattering terms. More details of the neutron radiography installation and imaging set-up will be presented in a forthcoming publication.

2.3.2 Fuel cell installation and operation. The passive PEMFC is fixed to an aluminum holder in front of the radial channel, with the possibility for vertical and horizontal cell position, i.e. main plane parallel and perpendicular to the gravity field, respectively. The vertical cell was studied under frontal and lateral irradiation. During acquisition of the neutron radiography, the cell is run at a fixed current (Keithley 2460 Sourcemeter), while supplied with dry hydrogen at 0.5 bar_g static pressure from a metal-hydride canister (Horizon Hydrostick Pro, 1 g H_2), and the static ambient air (22 °C, 30 % RH). Cell voltage and temperature are continuously recorded using a Keithley 2701 Multimeter with a 7700 multiplexer card. **Fig. 3** shows photographs of the set-up.

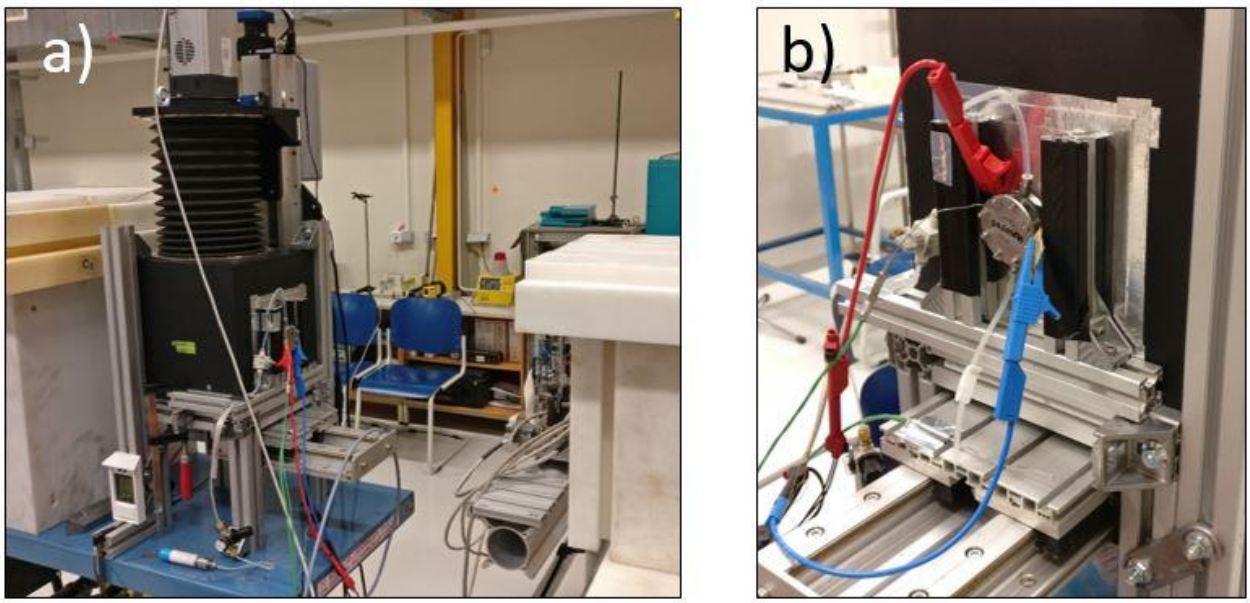

Fig. 3. a) Thermal neutron radiography set-up. b) Fuel cell installation.

Four cell configurations have been radiographed: vertical cell with frontal (1), and lateral (2) incidence, and horizontal cell with anode on top (3), and cathode on top (4). Fig. 3b shows the cell in configuration (1).

2.3.3. Image acquisition and processing. All neutron images were corrected for the dark-field and the flat-field. Dark-field correction consists of eliminating the pixel bias and the time-dependent dark current noise. With this aim, a series of images is taken with the camera shutter permanently closed. The recorded images are averaged resulting in the dark-field master image (*DF*). Correction for the neutron beam profile is handled via flat-fielding, by taking a series of images without any object in-between the neutron source and the detector, correcting their dark field as well, and averaging them (*FF*). The final image (*IM*) is obtained from the corrected neutron images (*NI*) according to:

$$IM = \frac{NI-DF}{FF-DF}\, m_{FF} \qquad \text{Eq. 1}$$

where m_{FF} is the calculated median (middle value separating the higher half from the lower half pixel sets) of the *FF* image. Averaging of a series of sub-exposure images, including *DF* and *FF*, was always performed by the median pixel of the series and without a 2D-Median Filter.

Neutron images were taken in-operando at different current demands. In each experiment, before starting images acquisition, the cell was dried by thorough spraying of compressed air over the cathode surface and through the anode chamber. The dried cell was then put in the holder and a first neutron image was taken to be used as dry-cell reference (IM_{dry}), consisting of five sub-exposure images. Then, the cell was started-up by increasing progressively the current demand in steps and simultaneous neutron images acquisition. Acquisition time for neutron image was 202 s (180 s sub-exposure and about 22 s readout time).

Images of the generated liquid water (IM_W) were obtained from the corrected fuel cell images (*IM*), by dividing by the reference, 'dry-cell', image (IM_{dry}), and taking the natural logarithm:

$$IM_W = \log\left(\frac{IM}{IM_{dry}}\right) \quad \text{Eq. 2}$$

To improve the signal-to-noise ratio and match the exposure time with IM_{dry}, moving averages of five consecutive images were computed. All digital image processing was carried out with the publicly available program ImageJ.

More information of the neutron imaging characteristics is given in Supplementary Information (S1), including the analysis of gray scale as a function of water produced in the cell, and the spatial resolution of the images.

3. Results and discussion

3.1 PEMFC polarization curves and impedance spectroscopy

3.1.1 Polarization curves. Polarization curves of the passive PEMFC are shown in **Fig. 4** for three cell orientations: vertical, horizontal cathode-down, and horizontal cathode-up. The curves were taken at 22 °C and 30 % RH under ambient static air, while feeding the dead-end anode with static dry H_2 (pressure 0.5 bar_g). The temperature of the cells during polarization curves acquisition was within 25 - 27 °C (see Supplementary Information, S2, Fig. S3), which is a result of its heat generation and dissipation to the surroundings. The curves show the best performance for the vertical cell with a maximum power density of 90 mW cm^{-2}, compared with 75 mW cm^{-2} for the horizontal cell. Little difference is observed between the cathode-up or -down in the horizontal cell. However, cathode-up leads to cell failure in constant current experiments (see next section).

Polarization curves of Fig. 4 have been analyzed with an analytical model for passive air-breathing PEMFC which accounts for changes in oxygen diffusivity inside the catalyst layer and the gas diffusion layer of the PEMFC cathode [38]. Details of the model, assumptions, and calculations are given in Appendix 1. Results of the fitting to the theory curve show that cell orientation is accompanied by a change in the oxygen diffusivity in the cathodic catalyst layer, from $8.0 \cdot 10^{-4}$ cm^2 s^{-1}, to $6.7 \cdot 10^{-4}$ cm^2 s^{-1}, and $6.5 \cdot 10^{-4}$ cm^2 s^{-1}, for the vertical, horizontal with cathode down, and horizontal with cathode up cell, respectively. In the gas diffusion layers, the calculated oxygen diffusivities are $145 \cdot 10^{-3}$ cm^2 s^{-1}, $109 \cdot 10^{-3}$ cm^2 s^{-1}, and $111 \cdot 10^{-3}$ cm^2 s^{-1} for vertical, horizontal cell with cathode down, and cathode up, respectively. The diffusivity values are gathered in **Table I**.

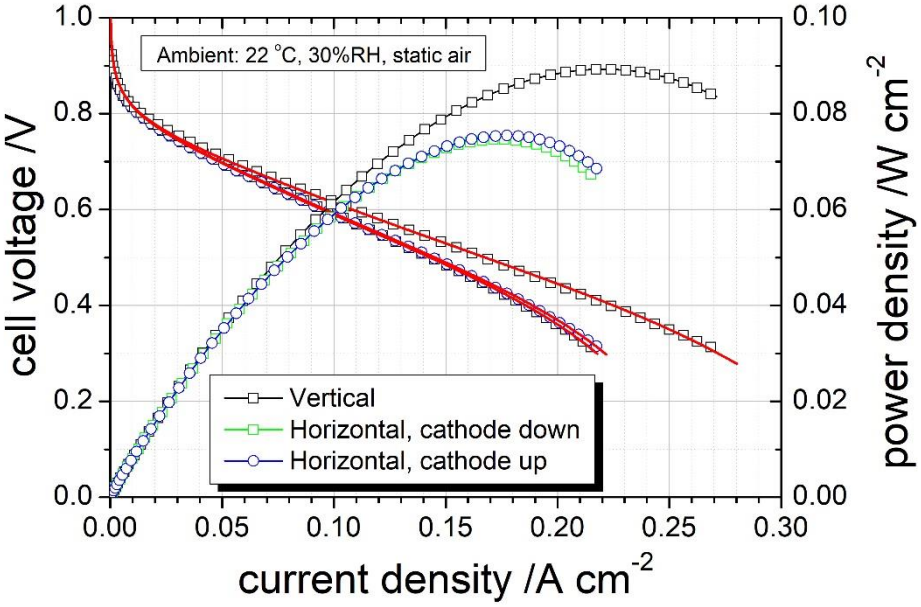

Fig. 4. Polarization curves and power density of the passive PEMFC in three different orientations. Cell supplied with dry H_2 in dead-end mode, and static ambient air. Pt loadings of anode/cathode: 0.25/0.30 mg cm^{-2}. Red line in polarization curves correspond to the best fit to the theory curve (Appendix 1).

Oxygen diffusivity changes of the porous layers can be related with changes in their water saturation (*s*), by using the expression [39]:

$$D_{eff} = D_{bulk} f(\varepsilon) g(s) \qquad \text{Eq. 3}$$

where D_{eff} and D_{bulk} are the effective diffusivity and the open space diffusivity, respectively, ε the porosity, $f(\varepsilon)$ is the ratio of the dry diffusivity of the film and D_{bulk}, and $g(s)$ is the ratio of D_{eff} and dry diffusivities of the film (dry diffusivity of the porous layer cancels out therefore in Eq. 3). Different expressions of $f(\varepsilon)$ and $g(s)$ have been proposed for the catalyst layer and the gas diffusion layer of a PEMFC electrode [39,40,41,42,43,44,45]. Taking for the gas diffusion layer the expression by García-Salaberri et al. [39], and for the catalyst layer by Zhen and Kim [45], the resulting water saturations for the layers of the cathode are given in Table I. The calculations assume laterally homogeneous layers, with the microporous carbon layer, present between the catalyst and the gas diffusion layers, included in the second one. Water saturation values in Table I show 35 % larger water content in the gas diffusion layer of the horizontal cell, while the catalyst layer saturation does not change much with cell orientation. It is also remarkable that the two horizontal positions, cathode up and down, present similar water saturation conditions in the two layers.

Table I. Diffusivities of the cathodic gas diffusion layer ($D_{eff,GDL}$) and catalyst layer ($D_{eff,CL}$), obtained from the analysis of polarization curves (Appendix 1), and water saturations ($s_{avg,GDL}$, $s_{avg,CL}$) calculated from Eq. 3, using expressions in foot notes (1) and (2) and $D_{bulk}=D_{O2-N2}$ = 0.20 $cm^2\ s^{-1}$ (1 atm, 20 ºC) [46]; ε_{GDL} = 0.75; ε_{CL} = 0.35.

Cell position	Vertical	Horizontal cathode down	Horizontal cathode up
$D_{eff,GDL}$ **/10^{-4} cm^2 s^{-1}**	145	109	111
$s_{avg,GDL}$ (1)	0.38	0.59	0.58

$D_{eff,CL}$ /10^{-4} cm^2 s^{-1}	8.0	6.7	6.5
$s_{avg,CL}$ (2)	0.71	0.73	0.73

(1) $f(\varepsilon)=\varepsilon^{3.5}$; $g(s) = (1-s)^{2.15}$ (ref. 39)

(2) $f(\varepsilon)=1.07\varepsilon^{1.75}$; $g(s) = (1-s)^{3}$ (ref. 45)

The analysis of polarization curves shows that cell orientation changes water saturation conditions in the cathode, mostly in its gas diffusion layer, and appears to be responsible for a 17 % decrease in peak power density for the horizontal with respect to the vertical cell. Impedance spectroscopy provides more information on transport limitations arising from changes in cell orientation.

3.1.2 Impedance spectroscopy. Plots of the imaginary part as a function of the real part of the impedance, or Nyquist plots (-Z'' vs. Z'), are shown in **Fig. 5** at two cell voltages and same cell orientations as in Fig. 4. A flattened single semicircle is observed in all cases which is due to the cathodic impedance of the cell [47]. Analysis of the spectra was carried out by fitting to an equivalent circuit (inset Fig. 5a), with a serial resistance (R_s) that accounts for high frequency ohmic losses, i.e. the ionic resistance of membrane and electrodes and electronic resistances, and a parallel combination of a resistor (R_1) and constant phase element (Y_1, n) that accounts for the low frequency losses. Resulting values of the fitting parameters are given in **Table II**, together with the steady-state cell temperature during the measurements.

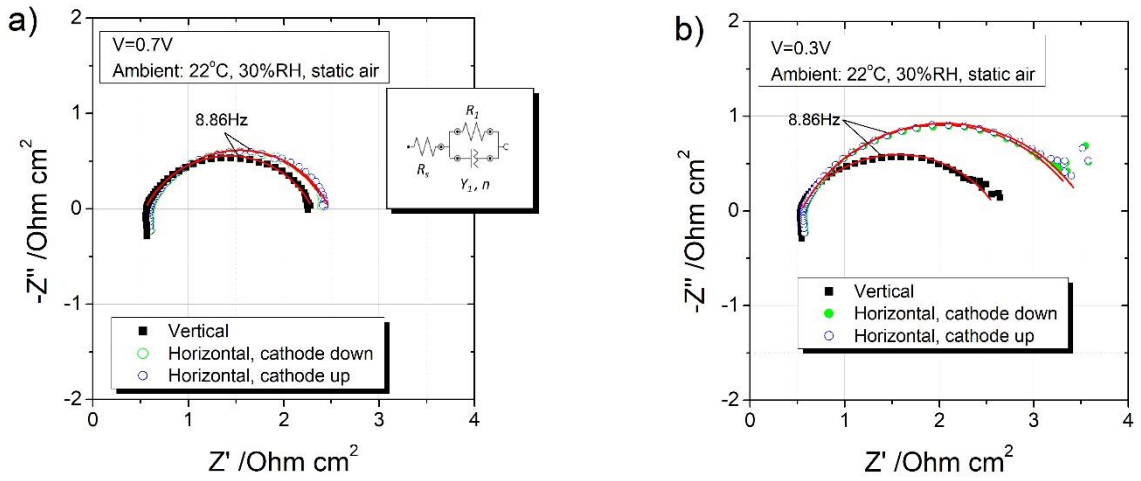

Fig. 5. Impedance spectroscopy on the passive PEMFC in three orientations, and two cell potentials, 0.7 V (a) and 0.3 V (b). In red the theory curve from the fitting to the circuit in the inset of Fig.5a.

Fitting results show 40 % increase in R_1, the low frequency resistor, by changing from vertical to horizontal cell position, at the lower cell voltage. There is also an increase at 0.7 V but to a minor extent. Changes in R_1 with cell orientation correspond with the diffusivity and water saturation changes inferred from the analysis of polarization curves. This parameter is attributed to the slow processes for current generation, predominantly related with the oxygen reduction in the cathodic catalyst layer, and with mass transport, normally liquid water, in the gas diffusion layer or other parts of the cell [47]. Since oxygen reduction kinetics accelerates at low cell voltage, due to favored charge transfer at increasing overvoltage, while the reverse is observed in Table II, it

can be concluded that R_1 predominantly reflects mass transport losses in the passive PEMFC, and explains the important increase by changing from vertical to horizontal position.

Additional information from the impedance spectroscopy analysis can be obtained from the other parameters in Table II. The constant phase element reflects the charge storage capability of carbon and platinum in the cathodic catalyst layer, and shows little variation with cell orientation. In fact, the associated effective capacitance, C_1^*, calculated from Y_1, n and R_1 (Table II) [48,49], which is proportional to the electrochemically accessible electrode area, remains almost unaltered by changing cell orientation. Finally, the serial resistance (R_s) shows a slight increase of 10 % for the horizontal cells, which must be attributed to the lower steady-state temperature attained before the impedance measurement.

Table II. Results of the impedance spectroscopy analysis (Fig. 5)

Cell Orientation	Vertical		Horizontal cathode down		Horizontal cathode up	
Cell voltage /V	0.7	0.3	0.7	0.3	0.7	0.3
Cell temp. / °C (1)	29	34	26	30	26	30
R_s /mOhm cm^2	550 (±4)	503 (±5)	595 (±4)	551 (±5)	589 (±4)	539 (±6)
R_1 /mOhm cm^2	1753 (±14)	2121 (±35)	1866 (±14)	2962 (±35)	1894 (±14)	3032 (±42)
Y_1 /mF s^{n-1} cm^{-2}	25 (±1)	45 (±2)	22 (±1)	32 (±1)	23 (±1)	32 (±1)
n	0.72 (±0.01)	0.65 (±0.01)	0.73 (±0.01)	0.70 (±0.01)	0.73 (±0.01)	0.70 (±0.01)
C_1^*/mF cm^{-2} (2)	7.5	12.8	6.7	11.4	7.1	12.1
χ^2	0.013	0.028	0.011	0.014	0.009	0.022

(1) Cell temperature attained during measurements by self-heating (ambient conditions: 22 °C, 30 % RH).

(2) Effective capacitance for normal to the surface time constant dispersion [48,49]: $C_1^* = Y_1^{1/n} \cdot R_1^{(1/n-1)}$

More insights into liquid water behavior inside the passive PEMFC can be gained with neutron radiography.

3.2 Neutron radiography

Neutron radiography was carried out on the passive PEMFC in vertical and horizontal orientations. For the vertical cell, images were acquired with frontal and lateral incidence. The H_2 inlet port position (up or down) was also tested in the vertical cell to register any possible influence of the H_2 flow on water distribution. Images of the horizontal were obtained under lateral neutron incidence, with cathode up and cathode down orientations.

Fig. 6 shows neutron radiographs of a cell in vertical position and under frontal incidence, with H_2 feeding through the down-port (Fig. 6a) and up-port (Fig.6b). The images were taken after generating different amounts of water (numbers indicated in the image in mg cm^{-2}), which appears as a spotted white contrast on the active area. The evolution of cell parameters (current, voltage, power, energy, water generation, and temperature) during the acquisition of the images are given in Supplementary Information, S3, Figs. S4 and S5.

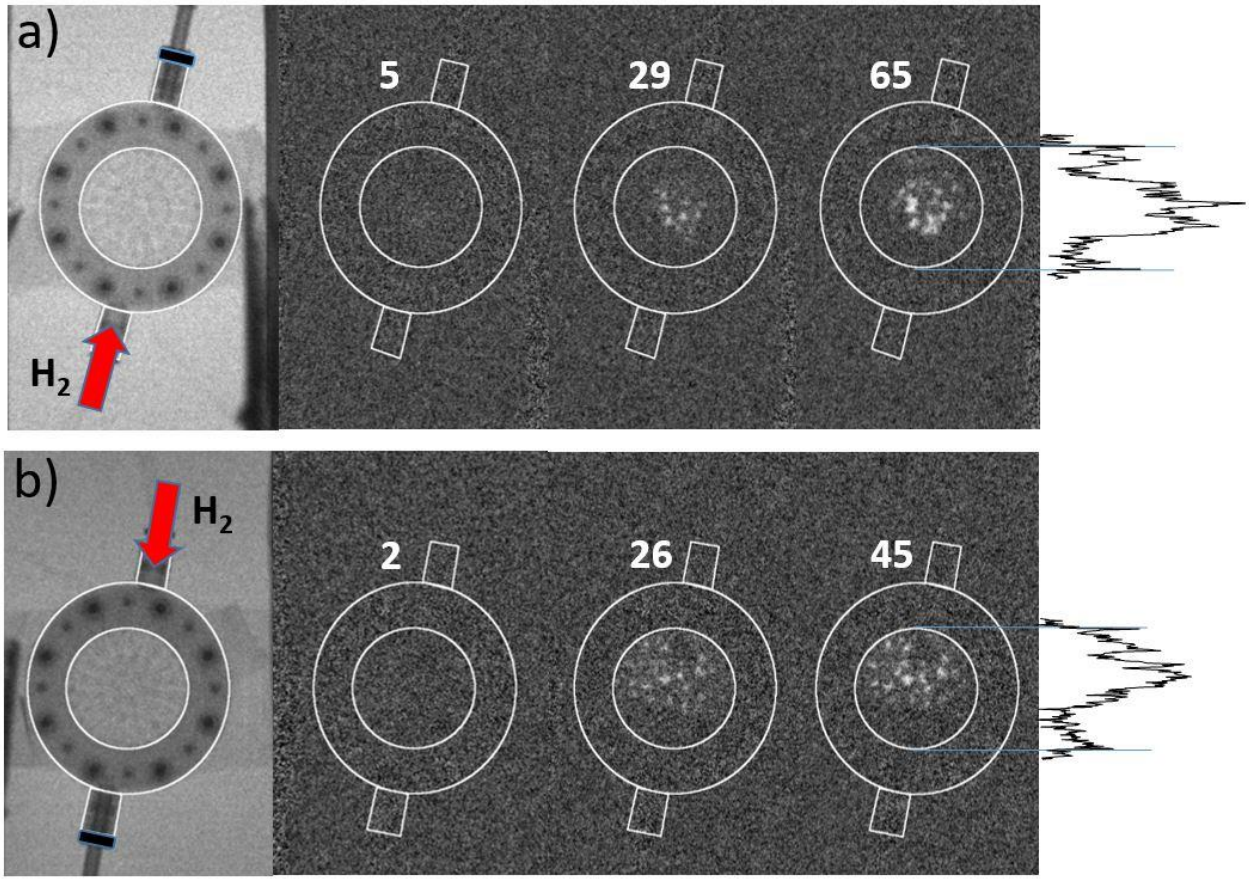

Fig. 6. Thermal neutron radiography under frontal incidence of the passive PEMFC in vertical position, with H_2 inlet from (a) down-port, and (b) up-port. The left image is the dry reference image (IM_{dry}, Eq. 2). Numbers indicate the amount of water produced by the cell in mg cm^{-2}. Cell active area, frame, and H_2 ports are drawn for visual guidance. Right: pixel values profiles taken over the center diameter of the active area.

The neutron images show liquid water accumulations preferentially centered in the active area of the cell with a slightly higher concentration in the upper half. The spotted distribution of water resembles the columns array of the cathodic plate, which, being more hydrophilic and colder than the electrode surface, favor condensation. In a similar way, preferential water accumulation is observed under the lands of flow field channels in conventional cells [39]. Water condensation deviation to the upper half of the active area can be explained by the combined effects of gravity and natural convection. The water droplets located in the lower half will leave the cell faster, also entrained by larger drops falling down from the upper half of the cell. Natural convection contributes to this asymmetry, since ambient air rising along the hot fuel cell will first “dry” the lower part of the cell thus reaching the upper half with a high vapor-content. In the extreme case, the lower cell part could even be dried-out such that the membrane-resistance increases, and leading to a smaller current density in the lower half of the cell, and therefore a locally reduced water production. The position of the inlet port, on the other hand, does not appear to include a significant difference in liquid water distribution.

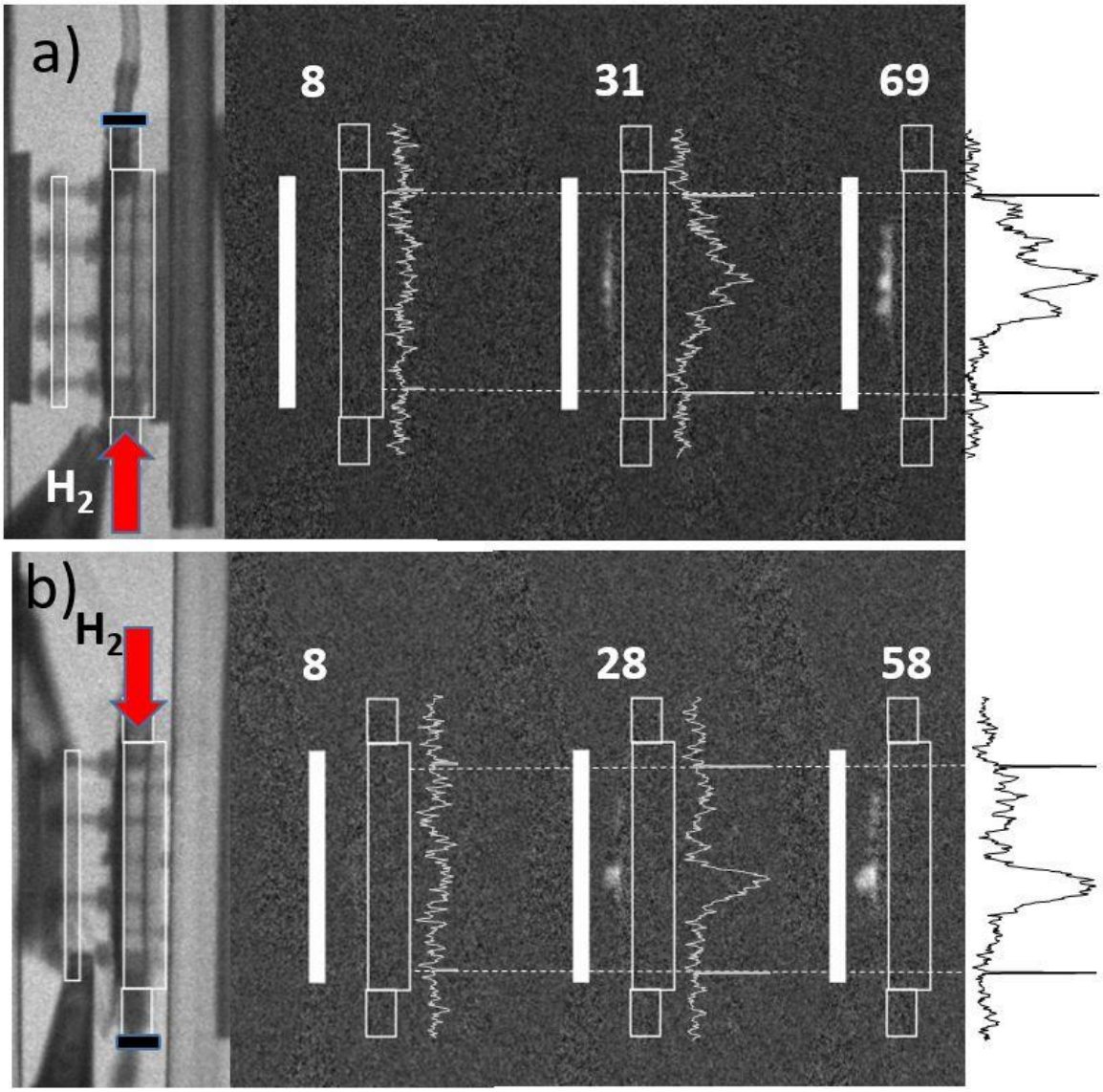

Fig. 7. Thermal neutron radiography images, and gray scale profiles, under lateral incidence in a passive PEMFC operating in vertical position, with (a) H_2 inlet from down-port, and (b) H_2 inlet from up-port. Numbers indicate the amount of water produced by the cell in mg cm^{-2}. Cathode plate (white bar), anode plate (empty bar), and H_2 ports are drawn for visual guidance. The left image is the dry reference image (IM_{dry}, Eq. 2).

Images of the vertical cell under lateral neutrons exposure are shown in **Fig. 7**, with the two different H_2 port locations (See Supplementary Information S3, Figs. S6 and S7, for cell parameters evolution during the acquisition). The images and gray scale profiles reflect preferential water accumulation in the central part of the active area, with larger accumulation in the upper half of the cathode surface than in lower areas, as observed in the frontal incidence image (c.f. Fig. 6).

Water concentration profiles as a function of cross sectional distance in the cell can be obtained from Fig. 7 images, as shown in **Fig. 8**, adding more profiles at intermediate and larger water generation. The profiles are obtained from the averaged gray levels over vertical slices covering the active area section. The location of different cell components is shadowed in Fig. 8 for reference.

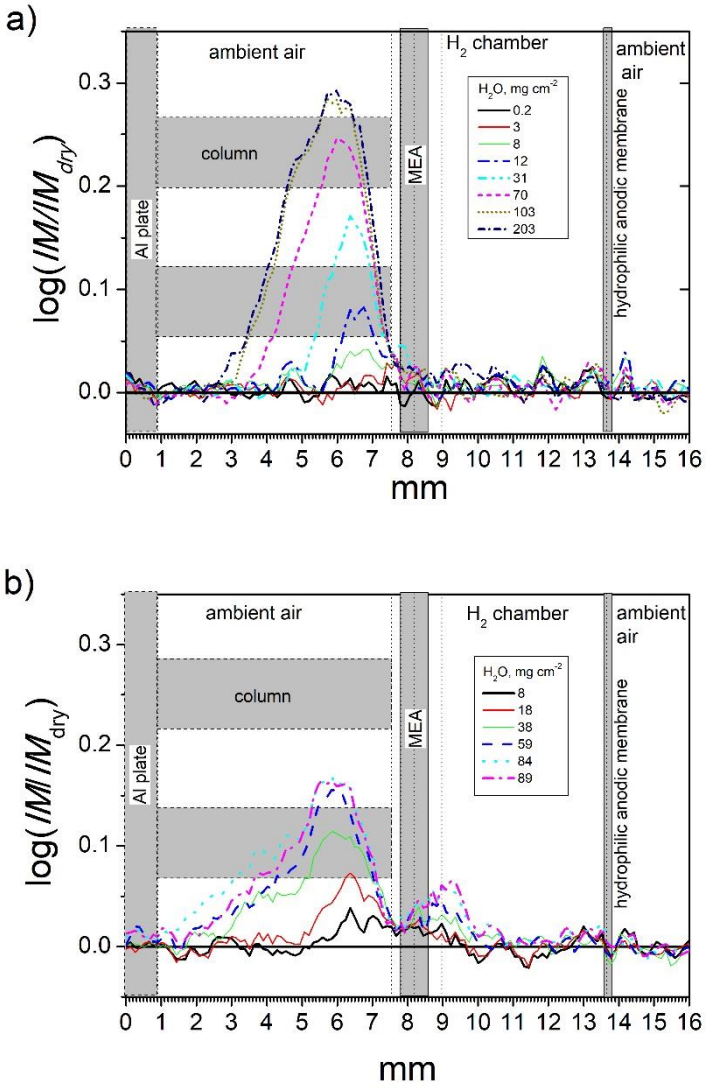

Fig. 8. Gray intensity vs. cross sectional distance in a passive PEMFC operating in vertical position, with H_2 inlet from (a) down-port, and (b) up-port, taken from neutron images in Fig. 7. Gray areas indicate the main components of the cell.

A steady-state profile is attained after about 70 mg cm^{-2} water generation, which corresponds with rather stabilization of cell voltage and temperature, at a current density above 0.2 A cm^{-2} (Supplementary Information, S3, Figs. S6 and S7). The profiles show the preferential water accumulation around the columns of the cathodic plate, reflecting the passive water removal from the cathode surface by the more hydrophilic and colder cathodic plate. Some anodic water accumulation is observed in the anode grid contact (grids are plotted as vertical dotted line in Fig. 8), especially in Fig. 8b, with H_2 feeding from the upper port. The MEA region appears to show a decrease in water concentration, which in fact reflects its decrease in volume concentration inside porous media highly saturated under operation (c.f. Table I), although the sensitivity of neutrons may also be different here. The hydrophilic anodic membrane, which is placed behind the anode grid to help passive water removal, shows minor water accumulation which may reflect effective permeation. It must be emphasized that the vertical cell, pictured in Figs. 6-8, is able to produce constant electricity for hours under full passive conditions, despite the important accumulation of liquid water observed on the cathode surface.

A different situation occurs when the cell is in horizontal position (**Fig. 9**). Two cases have been analyzed, cathode up (Fig. 9a), and cathode down (Fig. 9b). (See Supplementary Information for cells parameter evolution during images acquisition).

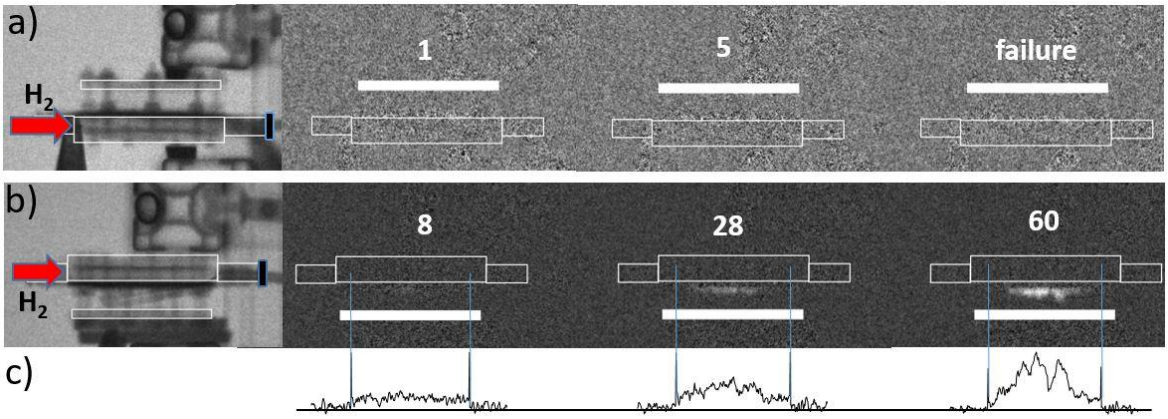

Fig. 9. Thermal neutron radiography images under lateral incidence in a passive PEMFC operating in horizontal position, with (a) cathode up, and (b) cathode down. Numbers indicate the amount of water produced by the cell in mg cm^{-2}. Cathode plate (white bar), anode plate (empty bar), and H_2 ports are drawn for visual guide. The left image is the dry reference image (IM_{dry}, Eq. 2). c) Plots of the gray intensity over the active area line.

Cathode up gives rise to a drop in voltage and cell failure shortly after production of 5 mg cm^{-2} of water. Therefore, no water accumulation can be observed in the neutron images with cathode up. With cathode down, however, the cell operates without failure; plots of the gray intensity over the active area (Fig. 9c) show uniform water generation from the initial profile (8 mg cm^{-2} water production), followed by preferential accumulation of large drops over central region of the cathodic plate after 60 mg cm^{-2} water production. Cross sectional water profiles extracted from Fig. 9 are plotted in **Fig. 10**.

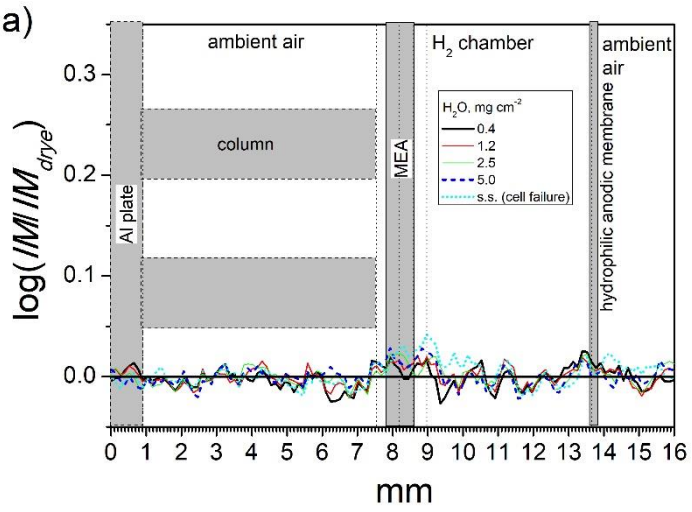

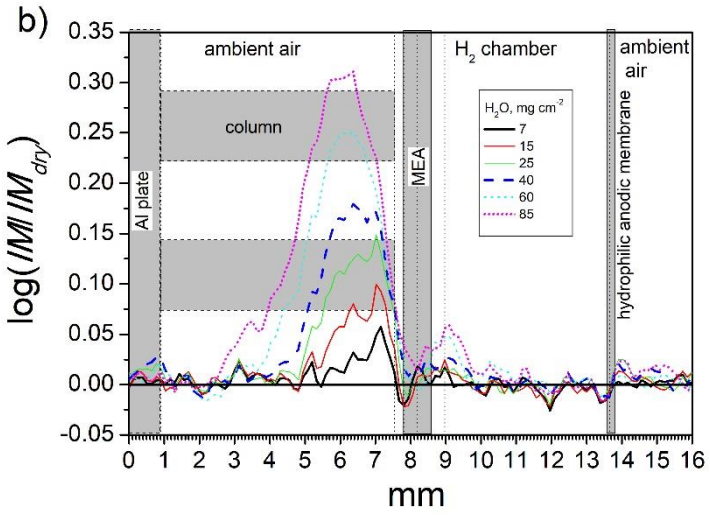

Fig. 10. Gray intensity vs. cross sectional distance in a passive PEMFC operating in horizontal position, with (a) cathode up, and (b) cathode down. Gray areas indicate the main components of the cell.

They show little water generation and accumulation with cathode up due to early failure of this cell after the production of 5 mg cm^{-2}. The cell returns to its full operative state after a short purging of the anode. With cathode down, no failure is observed and a water profile evolves in the cathode and anode, very similar to the profile of the vertical cell (c.f. Fig. 8) in spite their significant differences in polarization curves (Fig. 4) and impedance spectroscopy (Fig. 5).

4. Discussion

4.1 Power generation and passive PEMFC orientation

Polarization curves and impedance spectroscopy show an important influence of cell orientation on the performance of the passive PEMFC. It is in accordance with theoretical models of air-breathing cells that show their thermal dissipation favored by natural convective flows arising in vertical position [50,51]. The experimental studies carried out, however, show different results for the effect of cell orientation. An increase in cell performance in vertical position is reported by Jang et al. [52], when cathode plate has slits instead of circular openings for air admission. Obeisun et al. [53], using a cathodic plate with long horizontal openings, observed an effect by cell orientation only after prolonged operation time. The reason for the different results must be attributed to the characteristics of the cathodic plate. A plate design that allows for the movement of droplets over the cathode surface, as in the design by Jang et al. [52], gives rise to a favorable vertical cell orientation, whereas the design of by Obeisun et al. [53] accumulates static water drops on the cathode surface that are removed principally by evaporation.

Our cathodic columnar plate design must be included in the first type. In vertical position, lower water contents increases oxygen diffusivity in the cathode, resulting in larger peak power density compared with the horizontal position (Fig. 4). The changes in water contents and mass transport resistance with cell orientation occur by two principal natural forces acting on the passive PEMFC, namely the gravitational and natural convection. Gravitational rolling of water over the electrode surface in vertical position is important when single drops are large enough to overcome adhesion by

surface tension effects, which pin them to the cathode surface, current collector grid, and the columnar cathodic plate. Such water droplet removal is facilitated by hydrophobic elements that lower the adhesive forces. The natural convection caused by the "hot" fuel cell and oxygen/vapor concentration gradients [54] might even have more significant impact than gravitational dragging on liquid water removal. This phenomenon has been modelled by Ismail et al. [42], and experimentally observed by Fabian et al. [19] and Coz et al. [26]. For vertically aligned cells, a cold fluid particle rising in front of the hot GDE will be heated more and more as it rises, draining air from the surroundings and forming a strong upwards directed jet that enhances water evaporation from the cathode surface. The horizontally aligned fuel cell, however, resembles the classical Rayleigh-Bénard instability, where an air layer is heated from below, but natural convection will hardly reach the GDEs. As a result, the horizontal cell does not benefit from improved dragging of water and natural convection over the cathode surface.

The performance of a passive PEMFC is for this reason more dependent on orientation than for a conventional cell, where formation of small droplets on the surface of the gas diffusion layer and their dragging in the channels by the gas stream minimizes the effects of gravity and natural convection [55]. The passive cell performance relies on natural forces and water interaction with the surfaces of the electrode, grid contact, and columnar cathodic plate.

4.2 Water distribution in the passive PEMFC and cell performance

Water distribution profiles from neutron radiography give more insights into the behavior of the passive PEMFC, and explain the differences observed from vertical to horizontal positions. In spite of the similarity in water profiles of the vertical and horizontal cathode down positions observed from Figs. 8b and 10b, a closer view, almost in the limit of the resolution of the technique, allows to see differences that are most determinant for cell performance.

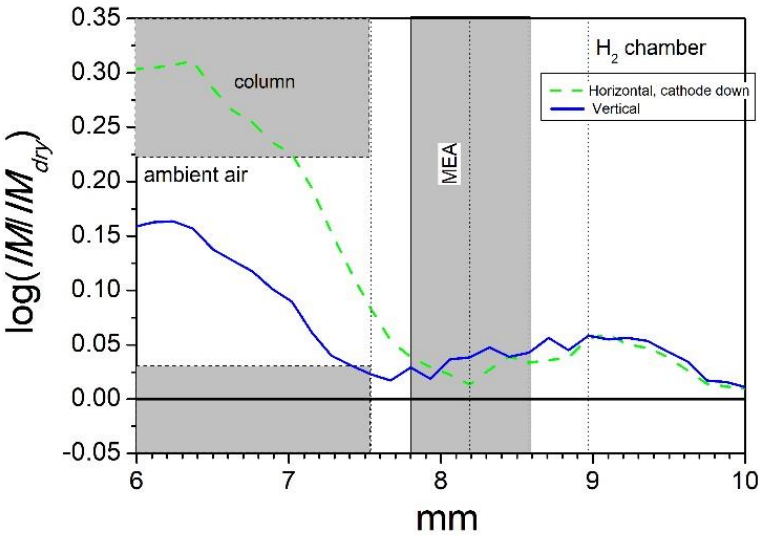

Fig. 11. Comparing the steady-state water profiles for vertical and horizontal cell with cathode down, after production of 85 mg cm^{-2} H_2O.

Fig. 11 shows the steady-state water profiles in the MEA region for a vertical and a horizontal cathode down cell. Principal differences start from the external part of the

cathode towards the grid collector and columnar plate. A steep rise from the cathodic side of the MEA towards the cathode surface and columnar plate reflects larger water contents in the cathode of the horizontal cell. The result is in accordance with the analysis of polarization curves (Table I). In the anode side, however, the water profiles are very similar for both orientations.

The changes in water distribution from cathode to anode and their dependence with cell orientation reflect the different nature of forces acting for water transport on both electrodes. In the cathode water transport is dominated by gravity and natural convection over the surface, which are very dependent on cell orientation. In the anode, water is driven by diffusion and capillarity, which are more insensitive to cell orientation. In fluid dynamics terms, the passive air breathing PEMFC is characterized by different Bond number in cathode than in anode (the Bond number, or Eötvös number, describing the relative importance of gravitational forces and surface tension). In the anode, it accomplishes Bo < 1, as in a conventional PEMFC electrode [55], whereas in the air-breathing cathode, Bo > 1.

Cell failure in horizontal position with cathode up can be explained from experimental data and neutron images. It is observed after production of a volume of water ($35 \cdot 10^{-3}$ cm^3) which amounts to 20 % of the open pores volume of the cathode. A deleterious effect by this small amount of water can only be explained by the flooding of a small, but critical part of the MEA, like the anodic catalyst layer. This situation is observed from a comparison of water profiles for the different cell orientations in the MEA region, as shown in **Fig. 12**.

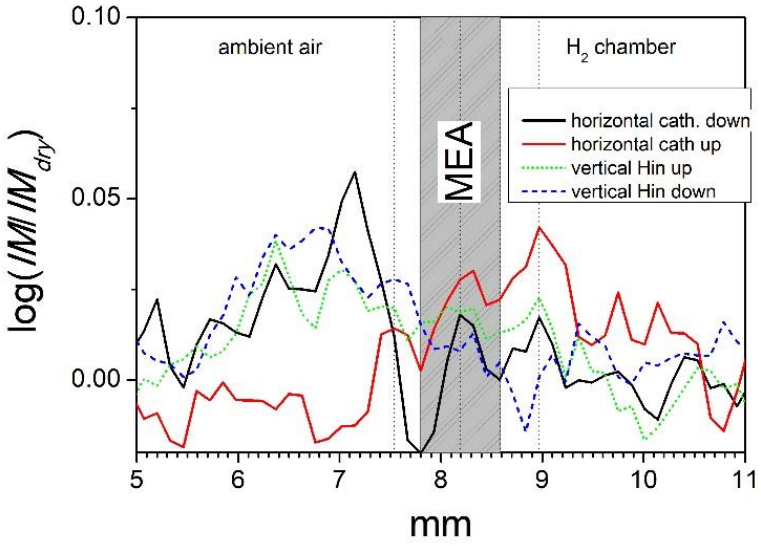

Fig. 12. Comparing water profiles after production of 5 mg cm^{-2} H_2O, for horizontal cells with cathode down and up, and for vertical cells with H_2 inlet down and up.

Fig. 12 shows that the profile after production of 5 mg cm^{-2} of water is different for the horizontal cell with cathode up than for the other three cells, characterized by larger water concentration in the anode side than in the cathode side. With cathode on top, gravity operates in favor of the back-diffusion transport of water to the anode, causing the flooding of its catalyst layer, which is critical due to the low solubility of hydrogen in water, and leads to immediate cell failure.

5. Conclusions

The following main conclusions can be obtained:

- Thermal neutron radiography at the AKR-2 (2 W) is able to resolve build-up of liquid water in the cathode and the anode of a passive air-breathing PEMFC.

- Liquid water accumulation is observed on the cathode and anode surface of the passive PEMFC.

- Cell orientation has a large influence on the response of the passive PEMFC, leading to 17 % increase in peak power density for a vertical cell with respect to a horizontal cell.

- Polarization curves analysis and impedance spectroscopy show that the horizontal cell presents larger mass transport losses due to higher water contents in the cathodic gas diffusion layer. Neutron imaging confirms more important water accumulation in the cathodic electrode of the horizontal cell.

- Water saturation changes with cell orientation are attributed to the different actuation on the cathode surface of two main natural forces: gravity and natural convection.

- Laying the cell horizontal with the cathode up produces eventual failure. In this position, back-diffusion and gravity operate in the same direction leading to flooding of the anodic catalyst layer.

Acknowledgements

This work was supported by the Ministerio de Economía y Competitividad of Spain, and Fondo Europeo de Desarrollo Regional (FEDER), Project E-LIG-E, ENE2015-70417-P (MINECO/FEDER).

References

[1] A. Heinzel, C. Hebling, M. Müller, M. Zedda, C. Müller, Fuel cells for low power applications, J. Power Sources. 105 (2002) 250–255. https://doi.org/10.1016/S0378-7753(01)00948-X.

[2] C.K. Dyer, Fuel cells for portable applications, J. Power Sources. 106 (2002) 31–34. https://doi.org/10.1016/S0378-7753(01)01069-2.

[3] J.S. Wainright, R.F. Savinell, C.C. Liu, M. Litt, Microfabricated fuel cells, Electrochim. Acta. 48 (2003) 2869–2877. https://doi.org/10.1016/S0013-4686(03)00351-7.

[4] J.P. Esquivel, F.J. Del Campo, J.L. Gomez de la Fuente, S. Rojas, N. Sabate, Micro Fuel Cells: Can We Apply Them to a Successful Market?, ECS Trans. 64 (2014) 875–880. https://doi.org/10.1149/06403.0875ecst.

[5] T.A. Thampan, D. Shah, C. Cook, S. Shah, Development and User Evaluation of an AlH3 Wearable Power System (WPS), ECS Trans. 65 (2015) 205–217. https://doi.org/10.1149/06501.0205ecst.

[6] T. Wilberforce, A. Alaswad, A. Palumbo, M. Dassisti, A.G. Olabi, Advances in stationary and portable fuel cell applications, Int. J. Hydrogen Energy. 41 (2016) 16509–16522. https://doi.org/10.1016/j.ijhydene.2016.02.057.

[7] Portable hydrogen energy systems: Fuel cells and storage fundamentals and applications, P. Ferreira-Aparicio, A.M. Chaparro (Editors), Elsevier, London, 2018. https://doi.org/10.1016/C2016-0-04605-3.

[8] J.P. Meyers, H.L. Maynard, Design considerations for miniaturized PEM fuel cells, J. Power Sources. 109 (2002) 76–88. https://doi.org/10.1016/S0378-7753(02)00066-6.

[9] B. Babcock, A.J. Tupper, D. Clark, T. Fabian, R. O'Hayre, Optimization of passive air breathing fuel cell cathodes, J. Fuel Cell Sci. Technol. 7 (2010) 0210171–02101711. https://doi.org/10.1115/1.3177381.

[10] M. Weiland, S. Wagner, R. Hahn, H. Reichl, Design and evaluation of a passive self-breathing micro fuel cell for autonomous portable applications, Int. J. Hydrogen Energy. 38 (2013) 440–446. https://doi.org/10.1016/j.ijhydene.2012.09.117.

[11] M. Weiland, P. Boillat, P. Oberholzer, A. Kaestner, E.H. Lehmann, T.J. Schmidt, G.G. Scherer, H. Reichl, High resolution neutron imaging for pulsed and constant load operation of passive self-breathing polymer electrolyte fuel cells, Electrochim. Acta. 87 (2013) 567–574. https://doi.org/10.1016/j.electacta.2012.09.091.

[12] G. Gautier, 'Micro fuel cells based on silicon materials', in 'Portable Hydrogen Energy Systems', Chapter 7, P. Ferreira-Aparicio, A.M. Chaparro (Editors),

Academic Press, Elsevier, London, 2018. https://doi.org/10.1016/C2016-0-04605-3.

[13] M.A. Folgado, J.J. Conde, P. Ferreira-Aparicio, A.M. Chaparro, Single Cell Study of Water Transport in PEMFCs with Electrosprayed Catalyst Layers, Fuel Cells. 18 (2018) 602–612. https://doi.org/10.1002/fuce.201700217.

[14] N. Karst, V. Faucheux, A. Martinent, P. Bouillon, J.Y. Laurent, F. Druart, J.P. Simonato, Innovative water management in micro air-breathing polymer electrolyte membrane fuel cells, J. Power Sources. 195 (2010) 1156–1162. https://doi.org/10.1016/j.jpowsour.2009.08.068.

[15] P. Ferreira-Aparicio, A.M. Chaparro, Novel dead-ended anode design for self-regulating humidification in an air-breathing H2-PEM fuel cell, ECS Trans. 64 (2014) 945–950. https://doi.org/10.1149/06403.0945ecst.

[16] CRC Handbook of Chemistry and Physics, 95th ed., Taylor & Francis, Boca Raton, 2014.

[17] S.U. Jeong, E.A. Cho, H.J. Kim, T.H. Lim, I.H. Oh, S.H. Kim, A study on cathode structure and water transport in air-breathing PEM fuel cells, J. Power Sources. 159 (2006) 1089–1094. https://doi.org/10.1016/j.jpowsour.2005.12.046.

[18] M. Paquin, L.G. Fréchette, Understanding cathode flooding and dry-out for water management in air breathing PEM fuel cells, J. Power Sources. 180 (2008) 440–451. https://doi.org/10.1016/j.jpowsour.2008.02.012.

[19] T. Fabian, J.D. Posner, R. O'Hayre, S.W. Cha, J.K. Eaton, F.B. Prinz, J.G. Santiago, The role of ambient conditions on the performance of a planar, air-breathing hydrogen PEM fuel cell, J. Power Sources. 161 (2006) 168–182. https://doi.org/10.1016/j.jpowsour.2006.03.054.

[20] J.B. Siegel, D.A. McKay, A.G. Stefanopoulou, D.S. Hussey, D.L. Jacobson, Measurement of Liquid Water Accumulation in a PEMFC with Dead-Ended Anode, J. Electrochem. Soc. 155 (2008) B1168. https://doi.org/10.1149/1.2976356.

[21] Y. Tabuchi, T. Shiomi, O. Aoki, N. Kubo, K. Shinohara, Effects of heat and water transport on the performance of polymer electrolyte membrane fuel cell under high current density operation, Electrochim. Acta. 56 (2010) 352–360. https://doi.org/10.1016/j.electacta.2010.08.070.

[22] S. Gößling, M. Klages, J. Haußmann, P. Beckhaus, M. Messerschmidt, T. Arlt, N. Kardjilov, I. Manke, J. Scholta, A. Heinzel, Analysis of liquid water formation in polymer electrolyte membrane (PEM) fuel cell flow fields with a dry cathode supply, J. Power Sources. 306 (2016) 658–665. https://doi.org/10.1016/j.jpowsour.2015.12.060.

[23] Q. Meyer, S. Ashton, S. Torija, C. Gurney, P. Boillat, M. Cochet, E. Engebretsen, D.P. Finegan, P. Adcock, P.R. Shearing, D.J.L. Brett, Nitrogen Blanketing and Hydrogen Starvation in Dead-Ended-Anode Polymer Electrolyte Fuel Cells Revealed by Hydro-Electro-Thermal Analysis, Electrochim. Acta. 203 (2016) 198–205. https://doi.org/10.1016/j.electacta.2016.04.018.

[24] N. Kulkarni, J.I.S. Cho, L. Rasha, R.E. Owen, Y. Wu, R. Ziesche, J. Hack, T. Neville, M. Whiteley, N. Kardjilov, H. Markötter, I. Manke, P.R. Shearing, D.J.L. Brett, Effect of cell compression on the water dynamics of a polymer electrolyte fuel cell using in-plane and through-plane in-operando neutron radiography, J. Power Sources. 439 (2019). https://doi.org/10.1016/j.jpowsour.2019.227074.

[25] A. Iranzo, J.M. Gregorio, P. Boillat, F. Rosa, Bipolar plate research using Computational Fluid Dynamics and neutron radiography for proton exchange membrane fuel cells, Int. J. Hydrogen Energy. 45 (2020) 12432–12442. https://doi.org/10.1016/j.ijhydene.2020.02.183.

[26] E. Coz, J. Théry, P. Boillat, V. Faucheux, D. Alincant, P. Capron, G. Gébel, Water management in a planar air-breathing fuel cell array using operando neutron imaging, J. Power Sources. 331 (2016) 535–543. https://doi.org/10.1016/j.jpowsour.2016.09.041.

[27] M. Siegwart, R.P. Harti, V. Manzi-Orezzoli, J. Valsecchi, M. Strobl, C. Grünzweig, T.J. Schmidt, P. Boillat, Selective Visualization of Water in Fuel Cell Gas Diffusion Layers with Neutron Dark-Field Imaging, J. Electrochem. Soc. 166 (2019) F149–F157. https://doi.org/10.1149/2.1011902jes.

[28] C. Hartnig, I. Manke, R. Kuhn, S. Kleinau, J. Goebbels, J. Banhart, High-resolution in-plane investigation of the water evolution and transport in PEM fuel cells, J. Power Sources. 188 (2009) 468–474. https://doi.org/10.1016/j.jpowsour.2008.12.023.

[29] H. Markötter, I. Manke, P. Krüger, T. Arlt, J. Haussmann, M. Klages, H. Riesemeier, C. Hartnig, J. Scholta, J. Banhart, Investigation of 3D water transport paths in gas diffusion layers by combined in-situ synchrotron X-ray radiography and tomography, Electrochem. Commun. 13 (2011) 1001–1004. https://doi.org/10.1016/j.elecom.2011.06.023.

[30] S. Prass, S. Hasanpour, P.K. Sow, A.B. Phillion, W. Mérida, Microscale X-ray tomographic investigation of the interfacial morphology between the catalyst and micro porous layers in proton exchange membrane fuel cells, J. Power Sources. 319 (2016) 82–89. https://doi.org/10.1016/j.jpowsour.2016.04.031.

[31] D. Muirhead, R. Banerjee, J. Lee, M.G. George, N. Ge, H. Liu, S. Chevalier, J. Hinebaugh, K. Han, A. Bazylak, Simultaneous characterization of oxygen transport resistance and spatially resolved liquid water saturation at high-current density of polymer electrolyte membrane fuel cells with varied cathode relative humidity, Int. J. Hydrogen Energy. 42 (2017) 29472–29483. https://doi.org/10.1016/j.ijhydene.2017.10.031.

[32] F.C. Cetinbas, X. Wang, R.K. Ahluwalia, N.N. Kariuki, R.P. Winarski, Z. Yang, J. Sharman, D.J. Myers, Microstructural Analysis and Transport Resistances of Low-Platinum-Loaded PEFC Electrodes, J. Electrochem. Soc. 164 (2017) F1596–F1607. https://doi.org/10.1149/2.1111714jes.

[33] R.T. White, S.H. Eberhardt, Y. Singh, T. Haddow, M. Dutta, F.P. Orfino, E. Kjeang, Four-dimensional joint visualization of electrode degradation and liquid water distribution inside operating polymer electrolyte fuel cells, Sci. Rep. 9 (2019). https://doi.org/10.1038/s41598-018-38464-9.

[34] J. Wu, X. Zi Yuan, H. Wang, M. Blanco, J.J. Martin, J. Zhang, Diagnostic tools in PEM fuel cell research: Part II. Physical/chemical methods, Int. J. Hydrogen Energy. 33 (2008) 1747–1757. https://doi.org/10.1016/j.ijhydene.2008.01.020.

[35] J. Bedet, G. Maranzana, S. Leclerc, O. Lottin, C. Moyne, D. Stemmelen, P. Mutzenhardt, D. Canet, Magnetic resonance imaging of water distribution and production in a 6 cm2 PEMFC under operation, Int. J. Hydrogen Energy. 33 (2008) 3146–3149. https://doi.org/10.1016/j.ijhydene.2008.01.053.

[36] S. Tsushima, S. Hirai, In situ diagnostics for water transport in proton exchange membrane fuel cells, Prog. Energy Combust. Sci. 37 (2011) 204–220. https://doi.org/10.1016/j.pecs.2010.06.001.

[37] C. Lange, N. Bernt, Neutron imaging at the low flux training and research reactor AKR-2, Nucl. Instruments Methods Phys. Res. Sect. A Accel. Spectrometers, Detect. Assoc. Equip. 941 (2019) 162292. https://doi.org/10.1016/j.nima.2019.06.033.

[38] P. Ferreira-Aparicio, A.M. Chaparro, Influence of the cathode catalyst layer thickness on the behaviour of an air breathing PEM fuel cell, Adv. Energy Res. 2 (2014) 73–84. https://doi.org/10.12989/eri.2014.2.2.073.

[39] P.A. García-Salaberri, J.T. Gostick, G. Hwang, A.Z. Weber, M. Vera, Effective diffusivity in partially-saturated carbon-fiber gas diffusion layers: Effect of local saturation and application to macroscopic continuum models, J. Power Sources. 296 (2015) 440–453. https://doi.org/10.1016/j.jpowsour.2015.07.034.

[40] R. Flückiger, S.A. Freunberger, D. Kramer, A. Wokaun, G.G. Scherer, F.N. Büchi, Anisotropic, effective diffusivity of porous gas diffusion layer materials for PEFC, Electrochim. Acta. 54 (2008) 551–559. https://doi.org/10.1016/j.electacta.2008.07.034.

[41] J.P. Owejan, T.A. Trabold, M.M. Mench, Oxygen transport resistance correlated to liquid water saturation in the gas diffusion layer of PEM fuel cells, Int. J. Heat Mass Transf. 71 (2014) 585–592. https://doi.org/10.1016/j.ijheatmasstransfer.2013.12.059.

[42] M.S. Ismail, D.B. Ingham, K.J. Hughes, L. Ma, M. Pourkashanian, Effective diffusivity of polymer electrolyte fuel cell gas diffusion layers: An overview and numerical study, Int. J. Hydrogen Energy. 40 (2015) 10994–11010. https://doi.org/10.1016/j.ijhydene.2015.06.073.

[43] S. Wang, Y. Wang, Investigation of the through-plane effective oxygen diffusivity in the porous media of PEM fuel cells: Effects of the pore size distribution and water saturation distribution, Int. J. Heat Mass Transf. 98 (2016) 541–549. https://doi.org/10.1016/j.ijheatmasstransfer.2016.03.060.

[44] S. Chevalier, J. Lee, N. Ge, R. Yip, P. Antonacci, Y. Tabuchi, T. Kotaka, A. Bazylak, In operando measurements of liquid water saturation distributions and effective diffusivities of polymer electrolyte membrane fuel cell gas diffusion layers, Electrochim. Acta. 210 (2016) 792–803. https://doi.org/10.1016/j.electacta.2016.05.180.

[45] W. Zheng, S.H. Kim, The Effects of Catalyst Layer Microstructure and Water Saturation on the Effective Diffusivity in PEMFC, J. Electrochem. Soc. 165 (2018) F468–F478. https://doi.org/10.1149/2.0711807jes.

[46] 'Transport processes in Chemically Reacting Flow Systems', D.E. Rosner. Dover Publication, Inc., New York, 2000.

[47] T.E. Springer, T.A. Zawodzinski, M.S. Wilson, S. Gottesfeld, Characterization of Polymer Electrolyte Fuel Cells Using AC Impedance Spectroscopy, J. Electrochem. Soc. 143 (1996) 587. https://doi.org/10.1149/1.1836485.

[48] C.H. Hsu, F. Mansfeld, Concernng the conversion of the constant phase element parameter Y0 into a capacitance, Corrosion. 57 (2001) 747–748. https://doi.org/10.5006/1.3280607.

[49] B. Hirschorn, M.E. Orazem, B. Tribollet, V. Vivier, I. Frateur, M. Musiani, Determination of effective capacitance and film thickness from constant-phase-element parameters, Electrochim. Acta. 55 (2010) 6218–6227. https://doi.org/10.1016/j.electacta.2009.10.065.

[50] M.S. Ismail, D.B. Ingham, K.J. Hughes, L. Ma, M. Pourkashanian, Thermal modelling of the cathode in air-breathing PEM fuel cells, 111 (2013) 529–537. https://doi.org/10.1016/j.apenergy.2013.05.007.

[51] Y. Zhang, R. Pitchumani, Numerical studies on an air-breathing proton exchange membrane (PEM) fuel cell, 50 (2007) 4698–4712. https://doi.org/10.1016/j.ijheatmasstransfer.2007.03.044.

[52] W.K. Jang, J. Choi, Y.H. Seo, B.H. Kim, Effect of Cathode Flow Field Configuration on Air- Breathing Proton Exchange Membrane Fuel Cell, Int. J. Precision Eng. Manufacturing 6 (2015) 1129–1134. https://doi.org/10.1007/s12541-015-0146-6.

[53] O.A. Obeisun, Q. Meyer, E. Engebretsen, D.P. Finegan, J.B. Robinson, G. Hinds, P.R. Shearing, D.J.L. Brett, ScienceDirect Study of water accumulation dynamics in the channels of an open-cathode fuel cell through electro-thermal characterisation and droplet visualisation, Int. J. Hydrogen Energy. 40 (2015) 16786–16796. https://doi.org/10.1016/j.ijhydene.2015.07.066.

[54] Y. Tabe, S-K Park, K. Kikuta, T. Chikahisa, Y. Hishinuma, Effect of cathode separator structure on performance characteristics of free-breathing PEMFCs, J. Power Sources 162(2006) 58-65.

[55] A. Mularczyk, Q. Lin, M.J. Blunt, A. Lamibrac, F. Marone, T.J. Schmidt, F.N. Buchi, J. Eller, Droplet and percolation network interactions in a fuel cell gas diffusion layer, J. Electrochem. Soc. (2020). https://doi.org/10.1149/1945-7111/ab8c85.

Appendix 1

A polarization curve for a passive air-breathing PEMFC which accounts for oxygen diffusivities in the cathodic electrode is described in Ref. 37. The latter is based on a one dimensional model for a flooded agglomerate porous catalyst layer, which considers both charge transfer kinetics and oxygen diffusion losses within pores. The model assumes macroscopically homogeneous electrode layers, the gas diffusion layer and the catalyst layer, with uniform overpotential distribution over the electrode thickness; the cathode kinetics is governed by first order oxygen reduction with Tafel behavior. The polarization curve obeys the general expression in Eq. A1 with three main potential losses, electrochemical (η_{ele}), ohmic (η_{ohm}), and mass transport (η_{mt}):

$$V = E - \eta_{ele} - \eta_{ohm} - \eta_{mt} \quad \text{(A1)}$$

Expressions for each overpotential term are determined as a function of current density. The electrochemical overpotential (η_{ele}) is due to the electrochemical reaction in the cathodic catalyst layer (no anodic polarization is considered). To calculate its relation with current density and oxygen diffusivity, the following expression is used:

$$D_{CL}\frac{d^2c(x)}{dx^2} = \frac{i(x)}{nF} \quad \text{(A2)}$$

Here, *c(x)* is the local oxygen concentration as a function of depth (*x,* see Eq. A4) in the catalyst layer, *i(x)* the local current density, D_{CL} is the effective diffusion coefficient of oxygen in the catalyst layer, *n*(= 4) the number of exchanged electrons per oxygen molecule, and *F*(= 96485 F mol^{-1}) the Faraday constant. The local current density (*i(x)*) depends on local oxygen concentration, electrochemical overpotential, and other kinetics parameters according to:

$$i(x) = \frac{c(x)}{c^0}\, A_i\, i_0\, exp\left(\eta_{ele}\frac{\alpha\, nF}{RT}\right) \quad \text{(A3)}$$

where A_i (cm^2 cm^{-3}) is the internal electrochemical area of the catalyst layer, i_0 (A cm^{-2}) the exchange current density, and α the transfer coefficient. Notice that positive signs are used for the overpotentials (as in Eq. A1) and for the reduction current; therefore the exponential term in Eq. A3 is also positive.

Eq. A2 is solved with boundary conditions at the membrane/CL (Eq. A4a) and CL/GDL (Eq. A4b) interfaces:

$x = L_{CL}$ $\quad$ d*c*/d*x* = 0 $\quad$ (A4a)

$x = 0$ $\quad$ $c = c^0$ $\quad$ (A4b)

where L_{CL} is the thickness of the catalyst layer, and c^0 is the oxygen concentration at the CL/GDL interface. Substitution of Eq. A3 into A2 and integration gives for the concentration profile:

$$c(x) = c^0\left(\frac{exp\left(2L_{CL}\sqrt{a}\right)+exp\left(2x\sqrt{a}\right)}{1+exp\left(2L_{CL}\sqrt{a}\right)}\right)exp\left(-x\sqrt{a}\right) \quad \text{(A5)}$$

where:

$$a = \frac{A_i\, i_0}{nFD_{CL}c^0}\; exp\left(\eta_{ele}\frac{\alpha\, n\, F}{RT}\right) \quad \text{(A6)}$$

The parameter $1/a^{1/2}$ is the penetration depth of the electrochemical reaction within the catalyst layer. The current profile (*i*(x)) and total current density (i_t) are given by:

$$i(x) = nF\, D_{CL} a\, c(x) \quad \text{(A7)}$$

$$\boldsymbol{i_t} = nF\, D_{CL} a \int_0^{L_{CL}} c(x) d(x) \quad \text{(A8)}$$

Integrating Eq. A8 gives for the total current:

$$\boldsymbol{i_t} = nF D_{CL} c^0 a^{1/2} tanh\left(a^{1/2} L_{CL}\right) \quad \text{(A9)}$$

The concentration at the CL/GDL interface, c^0, is obtained from the expression for a linear diffusion process in terms of gas diffusion layer parameters:

$$\boldsymbol{i_t} = nF\, D_{GDL} \frac{c^* - c^0}{L_{GDL}} \quad \text{(A10)}$$

where c^* is the oxygen concentration at the GDL/air, L_{GDL} the gas diffusion layer thickness, and D_{GDL} the effective oxygen diffusion coefficient in the GDL. For c^*, the dissolved concentration in water will be used depending on oxygen partial pressure (p_{O2}) through Henry isotherm:

$$c^* = k_H\, p_{O2} \quad \text{(A11)}$$

Here k_H (=1.2·10^{-6} mol cm^{-3} atm^{-1}) is the Henry isotherm constant of oxygen in water. Taking c^0 from Eq. A10 and substituting into Eqs. A6 and A9:

$$a = \frac{A_i\, i_0}{nF D_{CL}\left(c^* - \boldsymbol{i_t} \frac{L_{GDL}}{nF\, D_{GDL}}\right)}\ exp\left(\eta_{ele} \frac{\alpha\, nF}{RT}\right) \quad \text{(A12)}$$

$$\boldsymbol{i_t} = nF\, D_{CL} \frac{c^* \sqrt{a}}{coth\left(L_{CL}\sqrt{a}\right) + \frac{D_{CL}}{D_{GDL}} L_{GDL}\sqrt{a}} \quad \text{(A13)}$$

Eqs. A12 and A13 form a system of equations with two unknowns (a, $\boldsymbol{i_t}$), and with η_{ele} as parameter, which can be solved by iterative procedure, using $c^0 = c^*$ in Eq. A6 for the seminal a value.

The voltage loss due to mass transport within the GDL is expressed as a function of the current density and the diffusion limiting current (i_L):

$$\eta_{mt} = \frac{RT}{\alpha\, nF} log\left(\frac{i_L}{i_L - \boldsymbol{i_t}}\right) \quad \text{(A14)}$$

Finally, the ohmic overpotential is calculated according to:

$$\eta_{ohm} = \boldsymbol{i_t}\, R_{ohm} \quad \text{(A15)}$$

where the ohmic resistance (R_{ohm}) is due to electric contacts, specially between the grid collector and the cathode (R_{cont}), and the ionic resistances of the membrane and catalyst layers (R_{mem}, R_{CL}, respect.): $R_{ohm} = R_{CL} + R_{mem} + R_{cont}$

The thermodynamic potential in Eq. A1 (E) can be calculated as a function of temperature (T) and partial pressures of hydrogen and oxygen (p_{H2}, p_{O2}) from:

$$E = 1.229 - 0.85\ 10^{-3}(T - 298.15) + RT log(p_{H2}^2\, p_{O2}) \quad \text{(A16)}$$

Finally, the polarization curve in Eq. A1 results:

$$V = E - \eta_{ele} - \boldsymbol{i_t}\, R_i - \frac{RT}{\alpha\, nF} log\left(\frac{i_L}{i_L - \boldsymbol{i_t}}\right) \quad \text{(A17)}$$

The fitting to an experimental curve is carried out by first calculating the total current density, $\boldsymbol{i_t}$, for each η_{ele} by using the system of Eqs. A12 and A13, and then the other overpotentials and the cell voltage from $\boldsymbol{i_t}$ to obtain the polarization curve from Eq. A17.

The calculated diffusivities of the gas diffusion layer and catalyst layers, D_{GDL} and D_{CL}, for the three cell orientations are:

Cell orientation	$10^4 \cdot D_{CL}$ $cm^2\ s^{-1}$	$10^3 \cdot D_{GDL}$ $cm^2\ s^{-1}$	b(=2.303RT/αnF) V dec^{-1}	R_i Ohm cm^2	$10^4 \cdot X_i^2$
Vertical	8.0	145	0.097	0.45	5.5
Horizontal, cathode down	6.7	109			2.5
Horizontal, cathode up	6.5	111			2.6

Parameters b and R_i were first fitted and left unchanged for the three cell positions. Other common parameters used are:

A_i, electrocatalyst area of the cathodic catalyts layer, 60000 $cm^2\ cm^{-3}$ (measured by the hydrogen desorption technique)

c^*(=$k_{Henry}\ p_{O2}$), oxygen dissolved concentration in water, $0.25 \cdot 10^{-6}$ mol cm^{-3}

E^0, thermodynamic potential, 1.22 V (Eq. A.16)

i_0, exchange current density in cathode, $8.5 \cdot 10^{-9}$ A $cm^{-2}{}_{Pt}$

L_{CL}, cathodic catalyst layer thickness, 15 µm (measured SEM)

L_{GDL}, cathodic gas diffusion layer thickness, 400 µm (measured SEM)

p_{H2}, hydrogen pressure in anode, 1.5bar_g

p_{O2}, oxygen partial pressure in cathode, 0.21 bar_g

T, cell temperature, 298 K